A&A, 709, A249 (2026)
https://doi.org/10.1051/0004-6361/202558181

Astronomy & Astrophysics

A spectroscopic study of star clusters and compact emission-line nebulae in NGC 7793

E. Davoust[1], M. E. Sharina[2], and C. J. Donzelli[3,4,⋆]

[1] IRAP, Université de Toulouse, CNRS, 14 avenue E. Belin, F-31400 Toulouse, France
[2] Special Astrophysical Observatory, Russian Academy of Sciences, Nizhnii Arkhyz, KChR 36917, Russia
[3] Instituto de Investigaciones en Astronomía Teórica y Experimental (IATE (CONICET-UNC)), Córdoba, Argentina
[4] Observatorio Astronómico de Córdoba, Universidad Nacional de Córdoba, Córdoba, Argentina

Received 19 November 2025 / Accepted 9 April 2026

ABSTRACT

Context. Star clusters and emission-line nebulae are valuable probes of stellar populations and the chemical evolution of nearby galaxies. NGC 7793, the flocculent spiral in the Sculptor Group, contains a rich population of clusters and nebulae, although only a few absorption line objects have been studied spectroscopically so far.
Aims. Our goal is to confirm the membership of a selected sample of cluster and nebula candidates in NGC 7793 and to derive their main physical and chemical properties.
Methods. Candidates for globular clusters and planetary nebulae were selected using images from the *Hubble* Space Telescope (HST). Their structural and photometric parameters were determined. These candidates were then observed spectroscopically with Gemini–GMOS. Data were reduced with standard Gemini IRAF procedures. Structural parameters were measured on HST frames, and the stellar content of the clusters was analysed with full-spectrum fitting. Emission-line fluxes were used to estimate reddening, electron temperatures, and abundances for the nebulae.
Results. We confirm the presence of 19 star clusters and five H II regions associated with NGC 7793 based on their measured radial velocities and their spectroscopic, photometric, and structural properties. The clusters span a wide range of ages, from several Myr to about seven Gyr, and show metallicities between [Fe/H] ≈ −0.6 and +0.4. Their effective radii are typically 2–7 pc, comparable to those measured in other spiral galaxies of the Sculptor Group. All emission-line objects have spectra consistent with H II regions of sub-solar metallicity (12 + log(O/H) = 8.2–8.8).
Conclusions. This work provides a new spectroscopic census for the selected sample of star clusters and nebulae in NGC 7793. The properties of both populations are similar to those found in other late-type galaxies of the Sculptor Group.

Key words. galaxies: individual: NGC 7793 – galaxies: spiral – galaxies: star clusters: general

1. Introduction

Star clusters (SCs) of all ages are an essential tool for understanding the formation and evolution of galaxies and prototypical cases of stellar evolution, particularly of low-mass stars (Gratton et al. 2004). It is now clear that SCs are not single stellar populations and may contain several generations of stars, which in particular manifest themselves in the presence of horizontal branches with different morphologies and anti-correlations in the abundances of light elements (see, for example, Gratton et al. 2010; Mészáros et al. 2015). The interpretation of these peculiarities remains controversial. Detailed spectroscopic surveys of SCs in diverse galaxies are therefore crucial to establish whether galaxies share similar formation histories (Forbes et al. 2018), to determine whether the peculiarities observed in Galactic SCs are also present in other SC systems (Gratton et al. 2012).

NGC 7793 is the faintest of the five principal members of the Sculptor group. Its main characteristics from the catalog of Karachentsev et al. (2013) are summarized in Table 1. This galaxy is a flocculent spiral with substantial reservoirs of neutral hydrogen, CO, and H II regions, as well as a massive nuclear SC. Unlike many other low-mass spirals, NGC 7793 contains a hot halo 30% more extended than its stellar disk (He et al. 2025). Unlike M33, NGC 7793 is relatively isolated. Its nearest neighbor, NGC 55, lies at a distance of more than 400 kpc. This makes it a useful reference for studying SC populations formed without significant gravitational interactions.

Studies of SCs and emission-line (EL) nebulae in NGC 7793 made use of data from multiple facilities, including the *Hubble* Space Telescope (HST), the Atacama Large Millimeter/submillimeter Array (ALMA), and integral field spectroscopy. Previous works (Davidge 2016; Grasha et al. 2018; Della Bruna et al. 2020, 2021; Grasha et al. 2022) have derived the ages, masses, and spatial distributions of the SCs and EL nebulae in this galaxy, providing the basis for detailed studies of their connection to the interstellar medium (ISM). Building on these results, further research investigated the relationship between SCs and giant molecular clouds (GMCs), as well as the timescale over which star formation remains associated with these clouds. Spectra of H II regions linked to SCs have been used to assess how radiation from massive stars affects the surrounding gas (Della Bruna et al. 2021). These studies also examined how feedback from SCs, particularly supernovae, impacts the ISM and the escape of ionizing radiation. Integral field spectroscopy enabled a detailed analysis of the gas and stellar components in star-forming regions, including the use of diagnostic line ratios such as [S II]/Hα and [N II]/Hα. Young SCs show a strong spatial correlation with GMCs. Clusters

⋆ Corresponding author: carlos.donzelli@unc.edu.ar

Table 1. Main parameters of NGC 7793.

RA, Dec (J2000.0)	M_B	$\log(M_{26})$	$\log(M_{\rm HI})$	Diam	b/a	T	V_h	Dist	$(m-M)_0$
$23^h57^m49.4^s$, $-32°35^m24^s$	−18.5	10.28	8.77	14.13	0.68	6	227	3.91	27.96

Notes. The parameters are taken from Karachentsev et al. (2013). Columns list right ascension and declination, absolute B magnitude, logarithm of the mass within the Holmberg radius, logarithm of the H_I mass, major angular diameter (arcmin), apparent axial ratio, morphological type (numerical code following de Vaucouleurs et al. 1991), heliocentric radial velocity (km s^{-1}), distance (Mpc), and the corresponding distance modulus.

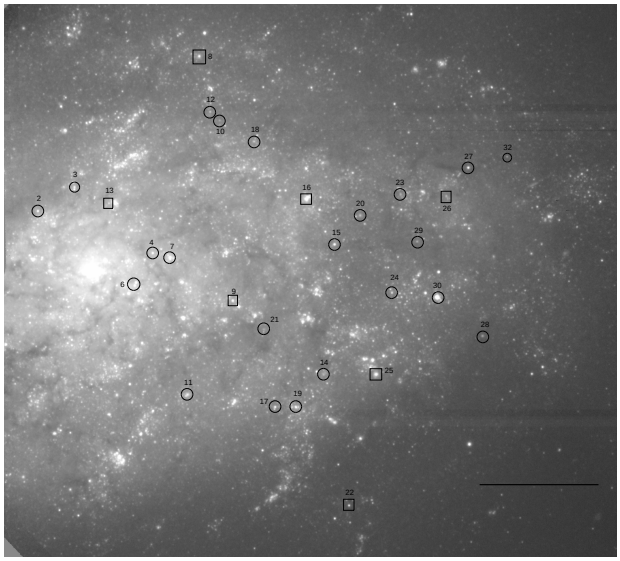

Fig. 1. Gemini pre-image. SCs are marked with circles, while EL nebulae are marked with squares. Numbers refer to slits. The image is 5×5 arcmin. North is at top and east to the left. The lower-right bar corresponds to 1 arcmin.

that remain physically associated with GMCs are typically younger than 11 Myr (Grasha et al. 2018). The age distribution of clusters increases with distance from the GMCs (Grasha et al. 2018), and SCs are generally more clustered than molecular clouds, suggesting a hierarchical structure in star formation (Della Bruna et al. 2020). Additional studies have revealed substructures in the abundance maps of H II regions surrounding clusters and massive stars, as well as variations in the ionization structure of H II regions, including the optical depth of the gas and the escape fraction of ionizing photons (Della Bruna et al. 2021). As a result, these studies have improved the understanding of the star formation process, the role of SCs in shaping the ISM, and the feedback mechanisms that regulate star formation in galaxies.

NGC 7793 is part of the Legacy ExtraGalactic UV Survey (LEGUS)[1], which provides HST photometry in the NUV, U, B, V, and I bands (Adamo et al. 2017). The properties of SCs (age, mass, $E(B-V)$, and metallicity) have been derived from HST photometry using stochastic stellar population synthesis models (Krumholz et al. 2015). Adamo et al. (2017) produced comprehensive automatic high-level young SC catalogs for a significant fraction of LEGUS galaxies, including NGC 7793. Adamo et al. (2017) performed a visual inspection to minimize contaminants in their final catalogs and added missed clusters. The total number of visually classified clusters in NGC 7793W is 299. Hannon et al. (2019) studied the Hα morphology of SCs.

Our study aims to determine the properties of a selected sample of SCs candidates in this galaxy, both young and old. It uses archival spectroscopic data for these objects, based on the list of cluster candidates compiled by the authors in 2010 from an analysis of HST images. In 2011, medium-resolution spectroscopy of these candidates was carried out using the Gemini South 8-meter telescope. The results of the analysis of these data will supplement the information available in the literature on the properties of stellar populations in NGC 7793.

We present the results in the following sections. Appendix A in the Appendix (available online) describes the SC candidate selection. In this section HST thumbnail images of the selected and observed objects are shown. Sect. 2 describes the observations and data reduction. In Sect. 3 we determine the photometric and structural parameters for the SC candidates using HST images. Sect. 4.1 presents the results of the analysis for objects with EL spectra. Sect. 4.2 presents the full-spectrum fitting results for objects with the absorption line spectra. The properties of the emission-line nebulae and star clusters are discussed in Sect. 5. Final remarks are given in Sect. 6.

2. Observations and data reduction

Spectra were obtained with the Gemini Multi-Object Spectrograph (GMOS), program GS-2011B-Q10 (PI: C. Donzelli). The observed field was placed toward the west side of the galaxy nucleus, covering a region of $\sim 5 \times 5$ arcmin^2, which corresponds to $\sim 6 \times 6$ kpc^2, assuming a distance to NGC 7793 of 3.9 Mpc. A multi-slit mask was created by the authors using a pre-image provided by Gemini. This image consisted of one 30 s exposure in the Sloan g filter. Given that the targets were selected using one of the fields surveyed by the Advanced Camera for Surveys onboard HST (see Appendix A, available online), our primary targets were located within an area of 202×202 arcsec west of the host galaxy nucleus. The central concentration limited the total number of targets that could be included in the GMOS slit mask. The mask was designed by the slit positioning algorithm (SPA), which determines which objects will be placed on the mask. Object selection is based on object priority and position on the frame, ensuring at least a 2-pixel separation between object spectra. Typically, around 30–40 slits can be placed on the mask depending on the width of the slit. In our case, the mask consisted of 35 slits, of which 28 were placed on SC candidates and 7 on EL nebulae candidates. Figure 1 shows the Gemini pre-image with the selected objects.

The spectroscopic data were acquired in queue mode on 30 November 2011 using the multi-slit mask. The slitlet dimensions were 1 arcsec by 4 arcsec. The grating used was the B600+_G5323, which has a ruling density of 600 lines/mm. Three pairs of exposures of 1800 s each were obtained with central wavelengths of 497, 502, and 507 nm. Thus, the science

[1] https://archive.stsci.edu/prepds/legus/dataproducts-public.html

targets had a total exposure time of ∼4 hours. The seeing was ∼0.9 arcsec during the observations. Spectra typically cover the wavelength range 3900–5600 Å, although, because the wavelength range depends on the position of the slit, some spectra start at ∼3600 Å, while others extend to ∼7000 Å. Flat fields, spectra of the standard star *LTT*9239, and the copper-argon lamp (CuAr) were also acquired to perform flux calibration. A binning of 2 × 2 was used, resulting in a scale of 0.1456 arcsec per pixel and a theoretical dispersion of ∼0.9 Å per pixel.

The coordinates of the observed object, location, classification, and comments on the projection proximity to brightest supernova remnants are listed in Table 2. Column 4 lists the deprojected distances from the centre of the galaxy in units of the galactic optical radius R_{25}. To calculate r/R_{25}, the measured galactocentric distances were corrected for the inclination of the NGC7793 disk to the line of sight and for the position angle as was done by Bibby & Crowther (2010). We used an inclination of 53.7° and the position angle of the major axis PA = 99.3° (Carignan & Puche 1990) and R_{25} = 4.65 arcmin (de Vaucouleurs et al. 1991). As a by-product of our study, we identified several supernova remnants (SNRs) from Blair & Long (1997) close to our objects in projection on the sky. The total number of SNRs in NGC 7793 found by Blair & Long (1997) in the optical is 27. Hundreds of X-ray SNRs are now known (Kopsacheili et al. 2025, and references therein). Apparently, every object in NGC 7793 has at some point been impacted by supernova ejecta.

All science and calibration files were retrieved from the Gemini Science Archive hosted by the Canadian Astronomy Data Centre. The data reduction described below was carried out using the Gemini IRAF package. Flat fields were derived with the task GSFLAT and the flat-field exposures. The spectra were reduced using GSREDUCE, which performs standard data reduction, including bias subtraction, overscan correction, cosmic ray removal, and application of the flat field derived with GSFLAT. GMOS-South detectors are read with three amplifiers, generating files with three extensions. The task GMOSAIC was used to produce data files with a single extension. The sky level was interactively removed using the task GSKYSUB, and the spectra were extracted using GSEXTRACT.

Flux calibration was performed using the spectra of the standard star LTT 9239, acquired with an identical instrument configuration. Spectra from *CuAr* lamps were obtained immediately after the science targets were observed and used for wavelength calibration with the task GSWAVELENGTH. The sensitivity function of the instrument was derived using GSSTANDARD and the reference file for LTT 9239 provided by the Gemini Observatory. The science spectra were flux-calibrated with GSCALIBRATE, which uses the sensitivity function derived by GSSTANDARD.

Table 2. Observed objects.

Slit	RA	Dec	r/R_{25}	Class, Notice
3	23:57:50.2	−32:34:46	0.25	SC
4	23:57:47.1	−32:35:19	0.14	SC[a]
8	23:57:45.3	−32:33:41	0.71	EL nebula
9	23:57:43.9	−32:35:43	0.27	SC[c]
10	23:57:44.5	−32:34:13	0.55	SC
11	23:57:45.7	−32:36:30	0.39	SC
12	23:57:44.8	−32:34:08	0.57	SC
13	23:57:48.8	−32:34:54	0.22	EL nebula
14	23:57:40.3	−32:36:20	0.50	SC
15	23:57:39.9	−32:35:15	0.48	SC[d]
16	23:57:41.0	−32:34:52	0.49	EL nebula[e]
17	23:57:42.3	−32:36:36	0.49	SC[f]
18	23:57:43.1	−32:34:23	0.54	SC
19	23:57:41.4	−32:36:36	0.52	SC
20	23:57:38.9	−32:35:00	0.56	SC
21	23:57:42.7	−32:35:57	0.35	SC[g]
22	23:57:39.3	−32:37:25	0.78	WN10[h]
23	23:57:37.3	−32:34:50	0.66	SC
24	23:57:37.6	−32:35:39	0.56	SC[i]
25	23:57:38.3	−32:36:20	0.57	EL nebula
26	23:57:35.5	−32:34:50	0.74	EL nebula
28	23:57:34.0	−32:36:00	0.73	SC
29	23:57:36.6	−32:35:13	0.63	SC
30	23:57:35.8	−32:35:41	0.64	SC[j]
32	23:57:33.0	−32:34:31	0.90	SC

Notes. Columns list: (1) slit number; (2) and (3) right ascension and declination (J2000); (4) deprojected distance from the centre of the galaxy; and (5) object classification based on our spectroscopic and photometric data analysis. [a]Whitmore et al. (2014)-002; within 5″ of SNR (Blair & Long 1997). [b]Within ∼12″ of SNR-4 (Blair & Long 1997). [c]Mora et al. (2009) 1-47 = Whitmore et al. (2014)-007. [d]Mora et al. (2009) 1-28. [e]Within ∼12″ of SNR-1 (Blair & Long 1997). [f]Mora et al. (2009) 1-18. [g]Within ∼4″ of SNR-4 (Blair & Long 1997). [h]Bibby & Crowther (2010). [i]Mora et al. (2009) 1-6. [j]Larsen (1999)-298 = Mora et al. (2009) 1-2.

3. Photometric parameters and half-light radii of the sample SC candidates

We have made use of images taken with the Advanced Camera for Surveys/Wide Field Channel (ACS/WFC), onboard the HST, under program 9774 (PI: Larsen) (see Mora et al. 2009, for more details). The images were downloaded from the Hubble Legacy Archive and correspond to the filters F435W, F555W, and F814W (hereafter *B*, *V*, and *I*). The pixel scale of ACS/WFC is 0.″05 pixel^{-1}, which corresponds to ∼1 pc, while typical SC sizes are a few pc. These files were pre-processed through the standard pipeline that corrects for bias, dark current, and flat field (Sirianni et al. 2005). Up-to-date photometric zero points yielding AB magnitudes were taken from the STScI website. The Galactic extinction value used for NGC 7793 is $E(B-V)$ = 0.021 mag, and the specific extinction corrections applied to each HST filter were obtained following the prescriptions of Sirianni et al. (2005), which give A_B = 0.086 mag, A_V = 0.067 mag, and A_I = 0.038 mag.

Aperture photometry for the observed objects was performed using DAOPHOT within IRAF. The total magnitudes were obtained through a series of circular apertures until the total flux converged. Before these calculations, a careful background subtraction was performed using an area with a radius of 5 arcsec around each object. In addition, neighboring objects were properly masked to avoid flux contamination. The total magnitudes calculated for the observed objects except those on slits 1, 2, 3, 33, 34, and 35, which are located outside the ACS images, are listed in Table 3.

We have also derived size estimates for the SCs, as has been done previously in other galaxies. In particular, Jordán et al. (2005) derived the half-light radii of SCs in about 100 early-type galaxies in the Virgo cluster. They report a median SCs half-light radius of 2.7 pc. Spitler et al. (2006) and Harris et al. (2010) report a median half-light of 3.2 pc for a sample of SCs in

Table 3. Photometric and structural parameters of the observed SCs and EL nebulae.

Slit	B	V	I	$R_{\rm eff}(B)$	$R_{\rm eff}(V)$	$R_{\rm eff}(I)$
4	19.87±0.12	19.67±0.11	19.82±0.12	1.91±0.20	2.00±0.21	1.86±0.19
8	20.22±0.15	19.60±0.10	21.44±0.18	–	–	–
9[a]	19.24±0.08	19.79±0.12	20.65±0.15	0.89±0.05	1.12±0.07	1.05±0.11
10	21.79±0.16	22.02±0.20	22.38±0.21	7.44±0.30	6.78±0.31	4.28±0.24
11	19.20±0.09	19.50±0.15	20.59±0.17	21.49±1.20	6.96±0.50	6.26±0.50
12	20.92±0.18	21.19±0.20	20.73±0.14	7.21±0.55	6.95±0.55	5.09±0.45
13	21.05±0.14	21.41±0.16	20.90±0.17	0.38±0.04	0.33±0.04	0.55±0.05
14	23.05±0.25	22.25±0.20	22.81±0.22	–	–	–
15[b]	19.22±0.09	19.72±0.11	20.57±0.15	3.60±0.25	3.85±0.24	3.52±0.24
16	18.78±0.09	19.10±0.10	20.33±0.14	–	–	–
17[c]	19.82±0.13	20.26±0.15	20.99±0.17	1.29±0.06	1.41±0.07	1.61±0.06
18	20.65±0.16	21.02±0.17	21.71±0.19	4.41±0.20	3.42±0.15	1.58±0.09
19	19.55±0.12	19.94±0.16	20.75±0.17	5.52±0.19	4.47±0.11	3.92±0.13
20	20.67±0.14	20.93±0.15	21.86±0.19	7.46±0.29	6.78±0.23	5.86±0.21
21	21.63±0.18	21.96±0.21	22.50±0.22	7.31±0.19	6.93±0.19	4.19±0.14
22	20.35±0.11	20.69±0.13	21.85±0.17	–	–	–
23	22.13±0.20	22.66±0.23	23.02±0.26	3.70±0.11	1.89±0.09	12.62±0.22
24[d]	20.32±0.11	20.89±0.14	21.99±0.19	2.38±0.12	2.52±0.13	3.63±0.16
25	19.21±0.09	18.91±0.07	20.44±0.11	–	–	–
26	21.56±0.15	22.07±0.21	23.02±0.26	–	–	–
28	21.45±0.16	21.28±0.14	21.57±0.17	10.92±0.30	16.75±0.43	–
29	21.27±0.13	21.55±0.15	22.39±0.21	5.00±0.21	6.23±0.19	5.96±0.19
30[e]	17.36±0.04	17.87±0.06	18.70±0.09	6.85±0.25	6.50±0.26	5.43±0.19
32	21.98±0.20	21.86±0.19	22.10±0.21	7.24±0.23	6.14±0.19	5.23±0.19

Notes. See Table 2 for object identification. Columns list: (1) slit number; (2), (3), and (4) total B, V, and I magnitudes; and (5), (6), and (7) effective radii in pc in the B, V, and I filters, respectively. Additional data from Mora et al. (2008): [(a)] $V = 19.85$, $E(B-V) = 0.17$, log(Age) = 6.77, $Z = 0.05$. [(b)] $V = 19.88$, $E(B-V) = 0.06$, log(Age) = 7.81, $Z = 0.008$. [(c)] $V = 20.33$, $E(B-V) = 0.12$, log(Age) = 7.39, $Z = 0.008$. [(d)] $V = 21.02$, $E(B-V) = 0.0$, log(Age) = 7.61, $Z = 0.008$. [e] $V = 18.19$, $E(B-V) = 0.22$, log(Age) = 6.64, $Z = 0.02$.

spiral galaxies. GCs in the Fornax and Sagittarius dwarf spheroidal galaxies in the Local group (LG) are on average larger. Their mean core radius is 5.1 pc (Table 5 in Mackey & Gilmore 2003). The corresponding half-light radius is even larger. The core radii of SCs in the Large and Small Magellanic clouds, the nearest dwarf irregular galaxies, grow with the SC ages (Sect. 5 and Fig. 5 in Mackey & Gilmore 2003). The dependence of the typical sizes of star clusters and their size dispersion on the luminosity and morphological type of the galaxy is still an open question. We fit the light profiles for our SCs candidates using ISHAPE (Larsen 1999), which convolves the point-spread function (PSF) with an analytical model of the surface brightness profile and searches for the best fit to the data by varying the full width at half maximum (FWHM) of the synthetic profile. We tried several analytical models such as King, Sérsic, and Gaussian. The model that best fits our data is a King profile with a concentration parameter of $c = 30$, defined as the ratio of the tidal radius to the core radius (King 1966). We built the PSF separately in each filter using the DAOPHOT package within IRAF, using stars across the field. The half-light radii for the SCs were obtained using the relation $R_{\rm eff} = 1.48({\rm FWHM}_{\rm King30})$ for all images (B, V, and I). On average, the effective radii are slightly larger in the B filter (5.1 ± 2.8 pc), compared to $R_{\rm eff} = 4.4 \pm 2.3$ in V and 4.8 ± 3.5 in I.

4. Spectroscopic data analysis

4.1. Emission-line objects

Some of the observed objects turned out to have emission lines in their spectra, suggesting that they are very young SCs or compact EL nebulae. Figure 2 shows the spectra of these objects, while Table B.1 (available online) shows the fluxes and equivalent widths for the emission lines and measured radial velocities.

Emission-line fluxes were obtained using the approach described by Kniazev et al. (2004).

Each emission line was then fitted with a single Gaussian on the continuum-subtracted spectrum. The uncertainties reported for the line intensities include contributions from Poisson noise of the line photons, errors in the continuum determination, which dominate for faint lines, and uncertainty in the spectral sensitivity calibration (~5%), which mainly affects strong lines. All contributions were finally combined in quadrature, and the resulting errors were applied to all derived quantities.

The logarithm of the ratios [O III] λ5007/Hβ, [N II] λ6584/Hα, and [S II] $\lambda\lambda$6716, 6731/Hα for the EL nebulae is given in Table 4. The missing values are due to the slit position in the mask, which causes the corresponding emission lines to be outside the spectral range.

According to Kniazev et al. (2008), the line ratios in the spectra of planetary nebulae (PNs), unlike those of H II regions, must satisfy at least one of the following criteria, namely Eqs. (1) and (2)

$$\log([{\rm O\,III}]/{\rm H}\beta) \geq (0.61/\log([{\rm O\,III}]/{\rm H}\alpha) - 0.47) + 1.19, \quad (1)$$

$$\log([{\rm S\,II}]/{\rm H}\alpha) \leq 0.63\ \log([{\rm N\,II}]/{\rm H}\alpha) - 0.55. \quad (2)$$

The criteria of Kniazev et al. (2008) assume that the main difference between a PN and an H II region is that the central star in a PN is much hotter than the OB stars ionizing H II

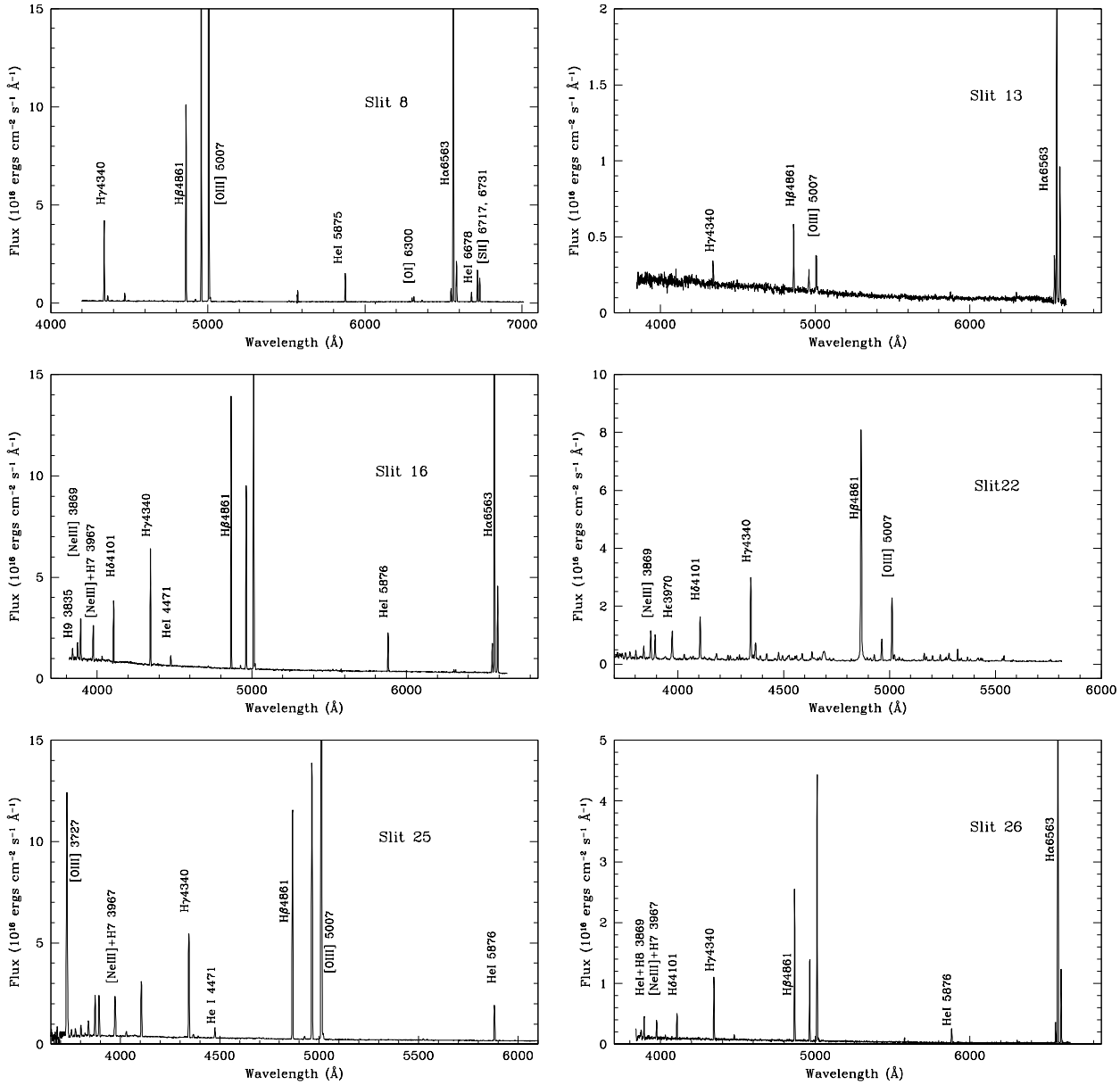

Fig. 2. Calibrated Gemini/GMOS spectra of the EL nebulae and the WN10 star (slit 22).

Table 4. Logarithmic emission-line ratios for the EL nebulae.

Object	log([O III]/Hβ)	log([N II]/Hα)	log([S II]/Hα)
Slit 8	0.69	−1.14	−1.40
Slit 13	−0.21	−0.35	–
Slit 16	0.31	−0.94	–
Slit 25	0.57	–	–
Slit 26	0.20	−0.75	–

regions. Slit 8 is the only object for which both criteria can be applied. This object does not satisfy the first criterion, but is classified as a PN according to the second one. For the remaining objects, none can be classified as PN according to the criterion (1). For slit 25, none of these criteria can be applied due to the absence of observable N II and S II emission lines in the spectra.

We derived several parameters describing the physical conditions and chemical abundances of the H II regions. In particular, we determined the extinction coefficient c(Hβ), the electron temperature, and the oxygen abundance for each emission-line object in our sample.

The extinction coefficient Hβ, c(Hβ) was obtained by comparing the observed Balmer line ratios with the Case B prediction [I(Hα)/I(Hβ) = 2.87], adopting the extinction law of Cardelli et al. (1989). When available, the mean value derived from the Hα/Hβ and Hγ/Hβ ratios was adopted.

The electron temperatures were measured directly using auroral lines. This was possible only for slit 8, where the [O III] λ4363 line was detected. For slit 25, where the spectral range allowed the detection of the [O II] λ3727 line, we applied the empirical relation derived from photoionization models by Stasińska & Izotov (2003). In particular, we used Eq. (1) of Izotov & Thuan (2007).

The oxygen abundance, expressed as 12 + log(O/H), was derived following the calibration of Denicoló et al. (2002). In

Table 5. Physical parameters of the sample objects.

Object	c(Hβ)	T_e [10^4 K]	12+log(O/H)	Rad. vel. [km s^{-1}]
Slit 8	0.41±0.04	1.02±0.02	8.20±0.03	307±11
Slit 13	1.21±0.09	–	8.77±0.53	257±11
Slit 16	0.38±0.05	–	8.35±0.21	345±17
Slit 25	–	1.52±0.01	8.45±0.06	318±12
Slit 26	0.15±0.05	–	8.49±0.10	353±15

only one case (slit 25), due to the limited spectral range, the calibration of Pilyugin & Thuan (2005, high branch) was adopted. We also used the same model to determine these values for slits 8, 16, and 26. In all cases, the calculated values are consistent, within the associated uncertainties, with those obtained using the Denicoló et al. (2002) method.

Table 5 shows the parameters calculated for these objects.

4.1.1. Comments for the individual EL nebulae

Slit 8. The spectrum has high excitation and shows a very high [O III]/Hβ ratio of 6.5. However, the He II λ = 4686 Å line is not detected. The reddening is moderate, c(Hβ) = 0.41 ± 0.04. The electron temperature derived from [O III] is 10 150 K, and 12+log(O/H) = 8.2. This value is quite similar to the average found by Della Bruna et al. (2021) (12+log(O/H) = 8.37 ± 0.25) in the interstellar medium of NGC 7793. Hβ has a large equivalent width (430 Å), indicating a source with strong nebular emission. These data suggest that the object could be an H II region with sub-solar metallicity. Unfortunately, the [O II] 3727 line lies outside the spectral range.

Slit 13. This object shows high extinction, c(Hβ) = 1.2, and the [O III]/Hβ ratio indicates a low-excitation spectrum. On the other hand, [N II]/Hα = 0.45 is relatively high. The measured metallicity is 12+log(O/H) = 8.77 ± 0.53. It is unlikely that this object is a PN given the low [O III]/Hβ ratio, and it is more likely a heavily reddened H II region.

Slit 16. Strong emission of the Hβ and [O III]/Hβ ratio > 2, together with low levels of [N II]/Hα suggest that this is an H II region photoionized by massive stars with high excitation and low metallicity, 12+log(O/H) = 8.35. The reddening is c(Hβ) = 0.38.

Slit 22. We identified the slit 22 as source number 8 in Table 2 of Bibby & Crowther (2010), who cataloged this object as a WN10 star.

Slit 25. The spectrum of this object is consistent with that of a low-metallicity H II region (12 + log(O/H) = 8.45). The reddening could not be determined because Hα is outside the observed spectral range. The electron temperature is high (15 200 K) and the ratio [O III]/Hβ is 5.1. A large equivalent width is also observed for Hβ (EW = 180). The He II λ = 4686 Å line is not detected. The ratios [N II]/Hα and [O III]/Hβ further support the classification of this object as a H II region.

Slit 26. This object also shows a spectrum consistent with that of a low-metallicity H II region (12+log(O/H) = 8.49). It exhibits a relatively low extinction, c(Hβ) = 0.14. Hβ has a considerable equivalent width (237 Å), indicating a young stellar population with strong emission.

In summary, none of the EL nebulae can be classified as PN. The non-detection of He II λ4686, together with the presence of neutral lines such as [O I] λ6300, confirms that these objects are regions H II rather than PN. We discuss the oxygen abundance gradient in Sect. 5.

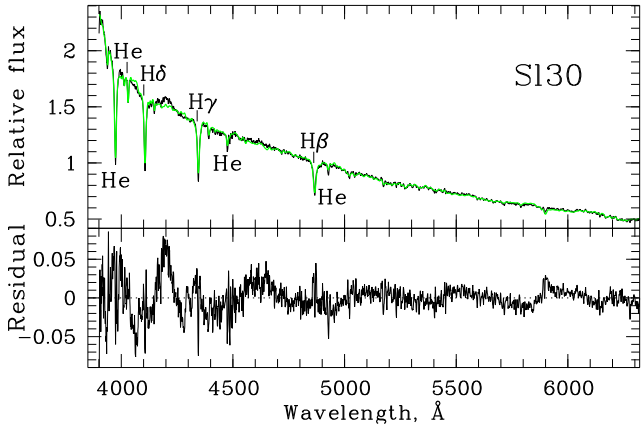

Fig. 3. Comparison of the Slit 30 spectrum of the SC Larsen (1999)-298 = Mora et al. (2009) 1-2 in NGC 7793 (black) with a composite model (green). Bottom: Difference between the observed and the model spectra (see Sect. 4.2 for details).

4.2. Full spectrum fitting results for the absorption line spectra

To derive radial velocities, metallicities, and ages of our objects, we used the ULySS package (Koleva et al. 2008, 2009) with the PEGASE-HR model grids (Le Borgne et al. 2004), the Salpeter IMF (Salpeter 1955), and the ELODIE stellar library (Prugniel & Soubiran 2001). ULySS performs a nonlinear least-square minimization between the observed and model spectra, while simultaneously normalizing the spectra and accounting for the spectrograph's line-spread function (LSF). Multiplicative and additive polynomials are applied to the observed spectrum to match the model spectrum (Prugniel et al. 2011). To extract kinematic information, we first determined the LSF spectrograph as in Koleva et al. (2008). The LSF was estimated by fitting a solar model spectrum to twilight spectra taken on the same night at the same field position. The fitting results for the SCs are given in Table 5 and Figs. 3, C.1, C.2, and C.3 (available online). Fig. 3 shows the highest signal-to-noise spectrum, that of the super SC 298 of Larsen (1999) (see Table 2), with the main spectroscopic features indicated.

The determined radial velocities, ages, and metallicities are presented in Table 6. All sample objects except Slit 3 are metal-rich. These findings are consistent with reports from the literature of active star formation on the disk of NGC 7793. The SCs on the Slits 3 and 4 appear to be old. In the next section, we will discuss these results in more detail. The derived radial velocities of the clusters (second column of Table 6) are compared with the Hα velocity field from Fabry–Perot observations by Dicaire et al. (2008) (see the middle-right panel of Fig. 1 in that paper). The approximate Hα velocities are listed in the fifth column of Table 6. Individual velocity differences (sixth column of Table 6) are on the order of our spectral velocity resolution (~0.9 Å/pix) or smaller. The mean value of $\mathrm{Vel_{obs}} - \mathrm{Vel_{H\alpha}}$ is -13 ± 31 km s^{-1}. This suggests that the majority of the SCs co-move with the ionized gas, which is expected given that most of the observed clusters are young.

Table 6. Spectroscopic results for the absorption-line spectra of SCs.

Slit	Vel_{obs}	Age	[Fe/H]	$Vel_{H\alpha}$	ΔVel
3	221±11	7066±168	−2.30±0.15	260	−39
4	283±13	2290±47	−0.26±0.09	270	13
9	258±7	13±0.3	0.36±0.05	275	−17
10	256±17	78±3.5	0.27±0.13	280	−24
11	262±9	379±8.3	0.02±0.08	260	2
12	323±12	178±4.5	−0.10±0.07	290	33
14	274±13	28±2.1	0.15±0.09	260	14
15	302±6	55±1.2	−0.29±0.06	300	2
17	282±9	32±1.3	−0.34±0.07	265	17
18	258±11	346±20	−0.59±0.09	280	−22
19	234±7	34±1.3	0.06±0.06	260	−26
20	328±12	385±12	−0.18±0.10	300	28
21	225±15	267±9.2	0.59±0.28	270	−45
23	253±9	29±5	−0.10±0.08	240	13
24	294±8	36±1.4	−0.38±0.06	275	19
28	265±11	391±11	−0.15±0.10	270	−5
29	230±13	295±8	0.06±0.08	300	−70
30	229±7	275±5	0.08±0.05	280	−51
32	254±10	397±13	0.54±0.09	300	−46

Notes. See also Table 2 and Sect. 4.2. Columns list: (1) slit number; (2) radial velocity in km s^{-1}; (3) age in Gyr; (4) [Fe/H] in dex; (5) Hα velocity from Dicaire et al. (2008) at the cluster position in km s^{-1}; and (6) difference between the observed and Hα velocities from Dicaire et al. (2008) at the cluster position in km s^{-1}.

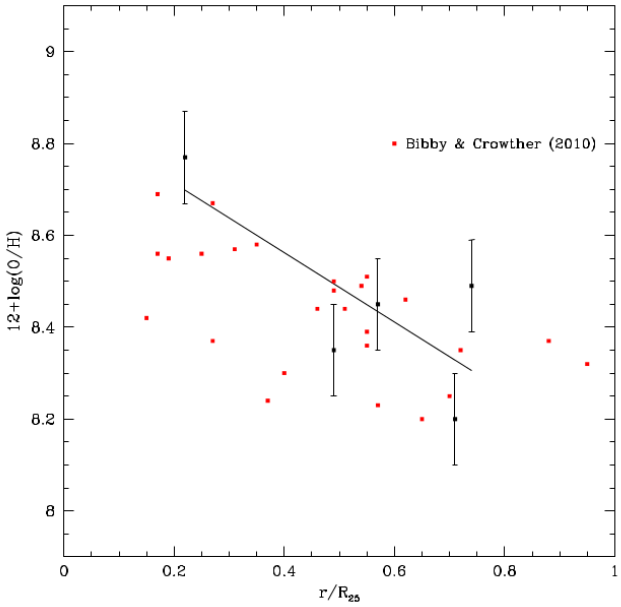

Fig. 4. 12+log(O/H) as a function of the galactocentric radius for the EL objects.

5. Discussion

5.1. Emission-line objects

The first catalogs of H II regions in NGC 7793 were compiled by Hodge (1969) and Davoust & de Vaucouleurs (1980). The latter determined the velocity field of the galaxy using Hα Fabry-Perot interferometry; they derived the rotation curve of NGC 7793 and estimated its mass. The authors established the absence of non-circular motions in the galaxy and noted that the spheroidal component contributes only 2–4 percent to the total mass.

No signatures of recent minor or major galaxy merging events were noticed by the analysis of the disk structure. However, 'the galaxy is expanding with a differential velocity of 4.9 km s^{-1} kpc^{-1} along the major axis. Such motion would cause a bending of the disk'. We note that such a bending might cause gas compression and heating, leading to an increase in the local gas density, which could explain the enhanced star-forming activity. Radburn-Smith et al. (2012) also found evidence for stellar migration in NGC 7793.

The diffuse emission of Hα in NGC 7793 was detected out to the edge of the HI disk and rotates in the same way as the HI disk (Dicaire et al. 2008). The rotation curve shows a decline. The ratio of dark to luminous mass is close to unity. This Keplerian rotation phenomenon has also been observed in S0 and actively star-forming galaxies. The interstellar matter in NGC 7793 is strongly ionized. The star formation rate of NGC 7793 is high compared to other nearby SA-type galaxies (Calzetti et al. 2015), with a value of 0.52 $M_{\odot}$ yr^{-1}.

The spectra of the EL nebulae allow us to determine the radial oxygen abundance profile. A linear regression to the measurements in slits 8, 13, 16, 25, and 26 yields a slope of −0.07 ± 0.02 dex kpc^{-1}. Figure 4 shows the result of the linear regression for our data. The plot also includes data from Table 4 of Bibby & Crowther (2010). Although our result is based on only five data points, it agrees well with the values reported by Dack & McCall (2012) (−0.086 ± 0.024) and Pilyugin et al. (2014) (−0.066 ± 0.010). Pilyugin et al. (2014) also report a central oxygen abundance 12 + log(O/H) = 8.50 ± 0.02 and a nitrogen abundance 12 + log(N/H) = 7.52 ± 0.05 with a nitrogen gradient of −0.163 ± 0.021 dex kpc^{-1}. Dack & McCall (2012) further describe the central abundance as close to solar. Similar values are found in other spirals of the Sculptor Group (e.g. Bresolin et al. 2009; Magrini et al. 2017; Westmoquette et al. 2011, for NGC 300, for NGC 55, and for NGC 253, respectively).

5.2. Absorption-line SCs

The distribution of the measured radial velocities of the SCs in NGC 7793 according to their galactocentric distances is shown in Fig. 5. The large symbols for the slit numbers denote objects with emission lines in the spectra (Table 5). The slit numbers of absorption-line objects younger than 100 Myr (Table 6) are indicated by small numbers in red. Absorption-line objects older than 100 Myr (Table 6) are shown with small black numbers in Fig. 5. Disk rotation (Dicaire et al. 2008) is shown schematically by the dashed line. Objects younger than 100 Myr move mainly with the ionized gas of the disk. The radial velocities of the older objects are closer to the systemic velocity of NGC 7793. However, there are exceptions to these trends among both older and younger groups of objects. The velocity scatter and the deviations in Fig. 5 likely argue in favor of the disk radial migrations of stars and SCs in NGC 7793.

Our spectroscopic study shows that most of the observed absorption-line SCs (Table 6) are young and metal-rich. Their radial distribution does not show a metallicity gradient. The central [Fe/H] value is close to the Solar one. Vlajić et al. (2011) found a positive metallicity gradient of old stellar populations in the outer disk of NGC 7793. These authors mention that this may be the indication of the inside-out disk formation scenario and of the radial stellar migrations in the disk. Vlajić et al. (2011) did not find a break in the red giant population in

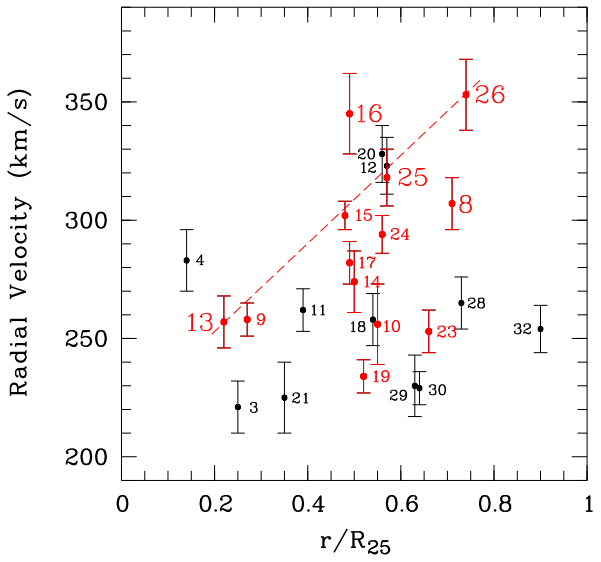

Fig. 5. Measured radial velocities of the studied objects with their slit numbers (see Tables 5, 6) as a function of the galactocentric radius (Table 2). Large red numbers indicate emission-line objects. Small red numbers indicate absorption-line objects younger than 100 Myr. Black numbers indicate absorption-line objects older than 100 Myr. Dashed red line shows disk rotation.

the outer regions of NGC 7793, i.e. the number of old stars diminishes evenly towards very large galactocentric distances. Radburn-Smith et al. (2012) found evidence of stellar migrations and of the presence of a thick disk and an old stellar halo in NGC 7793 by analyzing HST images. Our results agree with the above conclusions. In particular, the old objects Slit 3 and 4 projected near the centre of NGC 7793 may belong to the halo and to the thick disk, respectively.

6. Summary

Using GMOS archival observations we determined the following data: radial velocities, ages, and metallicities of 19 SCs with absorption-line spectra, as well as radial velocities and spectroscopic line properties for five observed objects with emission-line spectra. Using ACS/WFC HST images, we derived photometric and structural parameters for them. Because the radial velocities of the observed diffuse objects are close to the radial velocity of NGC 7793, we conclude that all of them belong to this galaxy. Almost all SCs studied appear to be young and metal-rich. We have not detected a radial metallicity gradient for the young absorption-line objects. SCs younger than 100 Myr move mainly with the ionized gaseous disk of NGC 7793. Older SCs have close to systemic radial velocities and are probably located in the thick disk or halo of NGC 7793. Deviations from disk rotation suggest that the SCs participate in the previously observed radial stellar migrations in NGC 7793 (Radburn-Smith et al. 2012).

We measured extinction coefficients, effective temperatures, oxygen abundances, and emission-line ratios for five compact EL nebulae and suggested that they are compact HII regions. None of our targets meets the criteria that are valid for PN according to Kniazev et al. (2008) or the classic diagnostic diagrams (Baldwin et al. 1981). We detected a negative oxygen abundance gradient among the five compact HII regions observed. This gradient is in good agreement with the values in the literature (Dack & McCall 2012; Pilyugin et al. 2014).

Flocculent galaxies tend to have lower bulge-to-total ratios, stellar masses, and surface densities compared to grand-design galaxies (Smith et al. 2024). However, as mentioned above, the disk of NGC 7793 is rich in supernova remnants, giant molecular clouds, star formation regions, and both ionized and neutral hydrogen. Star clusters in the disk or projected into the disk are visible in crowded star fields and cannot be confidently resolved into stars even using images obtained with space telescopes. All the information we have on the age and metallicity of SCs in NGC 7793 comes from analyzing their spectra. A complete census of globular clusters and their properties in NGC 7793 remains to be carried out.

Data availability

The complete Appendix (Appendices A and B), including HST postage-stamp images of the targets (Figs. A.1–A.3) and the full emission-line flux catalog (Table B.1), is available as supplementary material available at Zenodo (DOI: 10.5281/zenodo.19499010).

Acknowledgements. The Gemini data used in this paper were obtained under program GN-2011B-Q-10 through the Argentinian time share. This research has used NASA Astrophysics Data System Bibliographic Services (ADS), NASA/IPAC Extragalactic Database (NED), SIMBAD database, and Google. CJD thanks for Observatoire Midi-Pyrénées for its hospitality during this project. We thank the anonymous referee for their constructive comments, which helped improve the clarity and quality of this manuscript.

References

Adamo, A., Ryon, J. E., Messa, M., et al. 2017, ApJ, 841, 131
Baldwin, J. A., Phillips, M. M., & Terlevich, R. 1981, PASP, 93, 5
Bibby, J. L., & Crowther, P. A. 2010, MNRAS, 405, 2737
Blair, W. P., & Long, K. S. 1997, ApJS, 108, 261
Bresolin, F., Gieren, W., Kudritzki, R.-P., et al. 2009, ApJ, 700, 309
Calzetti, D., Lee, J. C., Sabbi, E., et al. 2015, AJ, 149, 51
Cardelli, J. A., Clayton, G. C., & Mathis, J. S. 1989, ApJ, 345, 245
Carignan, C., & Puche, D. 1990, AJ, 100, 394
Dack, S., & McCall, M. 2012, ApJ, 750, 167
Davidge, T. J. 2016, ApJ, 818, 142
Davoust, E., & de Vaucouleurs, G. 1980, ApJ, 242, 30
de Vaucouleurs, G., de Vaucouleurs, A., Corwin, Jr., H. G., et al. 1991, Third Reference Catalogue of Bright Galaxies (Springer-Verlag)
Della Bruna, L., Adamo, A., Bik, A., et al. 2020, A&A, 635, A134
Della Bruna, L., Adamo, A., Lee, J. C., et al. 2021, A&A, 650, A103
Denicoló, G., Terlevich, R., & Terlevich, E. 2002, MNRAS, 330, 69
Dicaire, I., Carignan, C., Amram, P., et al. 2008, AJ, 135, 2038
Forbes, D. A., Bastian, N., Gieles, M., et al. 2018, Proc. R. Soc. London Ser. A, 474, 20170616
Grasha, K., Calzetti, D., Bittle, L., et al. 2018, MNRAS, 481, 1016
Grasha, K., Chen, Q. H., Battisti, A. J., et al. 2022, ApJ, 929, 118
Gratton, R., Sneden, C., Carretta, E., et al. 2004, ARA&A, 42, 385
Gratton, R. G., Carretta, E., Bragaglia, A., Lucatello, S., & D'Orazi, V. 2010, A&A, 517, A81
Gratton, R. G., Carretta, E., & Bragaglia, A. 2012, A&A Rev., 20, 50
Hannon, S., Lee, J. C., Whitmore, B. C., et al. 2019, MNRAS, 490, 4648
Harris, W., Spitler, L. R., Forbes, D. A., et al. 2010, MNRAS, 401, 1965
He, L., Li, Z., Hou, M., et al. 2025, ApJ, 983, 149
Hodge, P. 1969, ApJS, 18, 73
Izotov, Y. I., & Thuan, T. X. 2007, ApJ, 665, 1115
Jordán, A., Côté, P., Blakeslee, J. P., et al. 2005, ApJ, 634, 1002
Karachentsev, I. D., Makarov, D. I., & Kaisina, E. I. 2013, AJ, 145, 101
King, I. 1966, AJ, 71, 64
Kniazev, A. Y., Pustilnik, S. A., Grebel, E. K., Lee, H., & Pramskij, A. G. 2004, ApJS, 153, 429
Kniazev, A. Y., Pustilnik, S. A., & Zucker, D. B. 2008, MNRAS, 384, 1045
Koleva, M., Prugniel, P., Ocvirk, P., Le Borgne, D., & Soubiran, C. 2008, MNRAS, 385, 1998
Koleva, M., Prugniel, P., Bouchard, A., & Wu, Y. 2009, A&A, 501, 1269
Kopsacheili, M., Anastasopoulou, K., Nanda, R., Gutierrez, C. P., & Galbany, L. 2025, A&A, 701, A60

Krumholz, M. R., Fumagalli, M., da Silva, R. L., Rendahl, T., & Parra, J. 2015, MNRAS, 452, 1447
Larsen, S. S. 1999, A&AS, 139, 393
Le Borgne, D., Rocca-Volmerange, B., Prugniel, P., et al. 2004, A&A, 425, 881
Mackey, A. D., & Gilmore, G. F. 2003, MNRAS, 340, 175
Magrini, L., Gonçalves, D. R., & Vajgel, B. 2017, MNRAS, 464, 739
Mészáros, S., Martell, S. L., Shetrone, M., et al. 2015, AJ, 149, 153
Mora, M., Larsen, S. S., Kissler-Patig, M., et al. 2008, A&A, 489, 1065
Mora, M., Larsen, S., Kissler-Patig, M., Brodie, J., & Ritchler, T. 2009, A&A, 501, 949
Pilyugin, L. S., & Thuan, T. X. 2005, ApJ, 631, 231
Pilyugin, L. S., Grebel, E. K., Zinchenko, I. A., & Kniazev, A. Y. 2014, AJ, 148, 134
Prugniel, P., & Soubiran, C. 2001, A&A, 369, 1048
Prugniel, P., Vauglin, I., & Koleva, M. 2011, A&A, 531, A165
Radburn-Smith, D., Roškar, R., Debattista, V. P., et al. 2012, ApJ, 753, 138
Radburn-Smith, D. J., Roškar, R., Debattista, V. P., et al. 2012, ApJ, 753, 138
Salpeter, E. 1955, ApJ, 121, 161
Sirianni, M., Jee, M. J., Benítez, N., et al. 2005, PASP, 117, 1049
Smith, B. J., Watson, M., Giroux, M. L., & Struck, C. 2024, AJ, 168, 12
Spitler, L. R., Larsen, S. S., Strader, J., et al. 2006, AJ, 132, 1593
Stasińska, G., & Izotov, Y. 2003, A&A, 397, 71
Vlajić, M., Bland-Hawthorn, J., & Freeman, K. C. 2011, ApJ, 732, 7
Westmoquette, M. S., Smith, L. J., & Gallagher, J. S., III 2011, MNRAS, 414, 3719
Whitmore, B. C., Chandar, R., Bowers, A. S., et al. 2014, AJ, 147, 78